Structure-function analysis of lithium-ion selectivity of voltage-gated sodium channel

Authors

Yuki K. Maeda[1,2], Kentaro Kojima[2], Tomoe Y. Nakamura[1], Toru Nakatsu[2], Katsumasa Irie[2]

1: Department of Pharmacology, Faculty of Medicine, Wakayama Medical University, Wakayama, Japan

2: Department of Biophysical Chemistry, Faculty of Pharmaceutical Sciences, Wakayama Medical University, Wakayama, Japan

Abstract

Voltage-gated sodium channels (Navs) selectively permeate Na^+ to generate action potentials. The efficiency of Na^+ permeation is known to be significantly higher than that of many other cations, but Li^+ can permeate Navs as much as Na^+. However, the molecular basis of the Li^+ permeation has been unclear. The ion selectivity of Navs is carried by the selectivity filter (SF) inside the ion pore. In this study, we performed mutagenesis of the SF and created prokaryotic Nav mutants with enhanced Li^+ selectivity. Electrophysiological and crystallographic analyses revealed the critical determinants for the enhanced Li^+ selectivity: the widened entrance of the SF allowing Li^+ to invade deeper into the SF without dehydration, the attraction of hydrated Li^+ by negative charges on the strong ion recognition site, and the smaller number of hydration water exchanges inside the SF. Additionally, the extensive interactions around the SF were shown to support ion permeation by stabilizing the ion pore. New drug directions based upon molecular basis for Li^+ permeation may target various neurological disorders and clarify the broader biological effects of lithium.

Introduction

Voltage-gated sodium channels (Navs) are integral membrane proteins that open by membrane potential depolarization (Hille, 2001). Navs conduct Na^+ ions inward quickly (~10^7 ions/sec) to initiate and propagate rapid action potentials (Catterall, 2023; Hodgkin & Huxley, 1952). The efficiency of Na^+ permeation of Nav is significantly higher than that of many other cations ($Na^+ \approx Li^+ \gg K^+, Cs^+, Ca^{2+}$), so Navs enable the Na^+ selective translocation across cell membranes in response to stimuli (Campbell, 1976; Hille, 1972; Pappone, 1980). This property makes Navs key players in nerve conduction, muscle contraction, secretion, neurotransmission, and many other processes. Alteration of the properties of the Navs causes a various pathological nervous conditions, including periodic paralysis, long QT syndrome, febrile convulsions, and epilepsy (Catterall, 2017; Jurkat-Rott *et al*, 2010; Lu *et al*, 2013; Rusina *et al*, 2024). Navs have therefore long been an essential target for drug design (Agwa *et al*, 2018; Bagal *et al*, 2015; Catterall *et al*, 2007; De Lera Ruiz & Kraus, 2015; England & De Groot, 2009).

The high Na^+ selectivity of Navs is well known, but Navs also permeate lithium ion (Li^+) with similar efficiency as with Na^+ (Hille, 2001). Although its physiological role are not fully understood, lithium has long been used as the first-choice drug for bipolar disorders (Cade, 1949; Shorter, 2009; Hart, 2024). Lithium preparations are still in use for the recurrence of prophylaxis and the acute treatment of manic, hypomanic, and depressive episodes in patients with bipolar disorder (Carvalho *et al*, 2015; Fountoulakis *et al*, 2016; Malhi *et al*, 2015; Nestsiarovich *et al*, 2022; Verdolini *et al*, 2021). Li^+ in the blood, liberated from lithium chloride, is assumed to enter cells via Navs (Timmer and Sands, 1999) and it apparently exerts its effects on various cellular systems (Hart, 2024; Schrauzer, 2002). While the beneficial biological effects of lithium are known, concerns have also been raised about bioaccumulation toxicity (Chevalier *et al*, 2024). Environmental lithium concentrations are increasing due to its medical use, and the recent massive consumption of industrial products such as Li^+ batteries. Reported harmful effects include neurological disorders, immune disorders, cardiovascular diseases, enuresis and polydipsia, fetal diseases, and neurodevelopmental effects of the thyroid hormone system (Chevalier *et al*, 2024). These beneficial and adverse biological effects of lithium are well summarized (Bortolozzi *et al*, 2024; Chevalier *et al*, 2024; Hart, 2024). However, there are few reports on the mechanism by which Li^+ enters the cell, i.e., the molecular mechanisms by which Li^+ permeates Navs.

Na^+ and Li^+ have different ionic properties, so it is uncertainty about how they achieve comparable ion permeability in Navs. In mammalian Navs, the pore-forming subunit (α_1) consists of four repeats, which are formed by six-fold transmembrane segments (S1-S6)

in each repeat (Abriel & Kass, 2005; Catterall, 2000). Each repeat consists of two domains: S1-S4 detects membrane voltage as the voltage-sensing domain, and S5-S6 builds the ion pore by facing each other four as the pore domain. The pore module in the center of ion channels consists of an outer funnel-like vestibule, a selectivity filter (SF), a central cavity, and an intracellular activation gate. The permeation efficiency of each ion is mainly determined by the five amino acid residues of the SF, which narrow the ion pore the most. (Hille, 2001). mutagenetic and structural analyses have confirmed that the charged side-chain site (Asp-Glu-Ala-Lys [DEKA]) in the SF is critical for ion permeability (Favre *et al*, 1996; Schlief *et al*, 1996; Jiang *et al*, 2020). Nevertheless, the asymmetric and tortuous configuration of vertebrate Navs makes it challenging to understand the full extent of ion permeation processes.

As a substitute for vertebrate Navs, the mechanism of Na^+ permeation in the SF of Navs is well explained by the functional analyses and three-dimensional structures of several bacterial Navs (BacNavs) (Ahern *et al*, 2016; Corry & Thomas, 2012; Payandeh *et al*, 2011). BacNavs comprise homo-tetramers of subunits with a structure that resembles a repeat of vertebrate Navs. Based on phylogenetic analysis, the lineage of BacNavs likely diverged from a progenitor of eukaryotic Navs and voltage-gated calcium channels (Cavs), and the structural features are conserved in each other (Catterall & Zheng, 2015; Liebeskind *et al*, 2013; Zakon, 2012). BacNavs have been used as models for the molecular basis of ion channels because of the simple relationships between functions and structural changes. Especially for the SF, mutations into the BacNavs monomer simultaneously substitute the four facing residues in its homo-tetramer, leading to dynamic changes in ion permeation. Importantly, BacNavs also permeate Li^+ as well as eukaryotic Navs (the permeation ratio of Li^+ over Na^+ is 0.6~0.8 in BacNavs and is 0.9~1.1 in eukaryotic Navs) (DeCaen *et al*, 2014; Finol-Urdaneta *et al*, 2014; Naylor *et al*, 2016; Hille, 2001). We therefor thought that if BacNav mutants with enhanced Li^+ selectivity were created, it might be possible to identify the critical factors of the permeation of Li^+ common to eukaryotic Navs.

In this study, we succeeded the creation of a Li^+-selective BacNav mutant ,which has never been reported before. Its series of mutants had gradational enhanced Li^+ selectivity in electrophysiological analyses. Furthermore, crystallography showed the key to improving Li^+ selectivity: the widened entrance of the SF allowing hydrated ions to invade deeper to the SF, the interaction of ions with the strong ion recognition site in closer proximity, and the smaller number of hydration water exchanges during passage through the SF. This is thought to be the first study of the structural basis of the interaction between Navs and permeating Li^+. This insight into the mechanisms by which Li^+ enters

cells could lead to improved treatments for various neurological disorders and greater understanding of the biological effects of lithium.

Methods

Site-directed mutagenesis and construction of NavAb mutants

DNA constructs were produced as previously reported (Irie *et al*, 2023). The NavAb mutated DNAs were subcloned into the modified pBiEX-1 vector (Novagen; 71234-3CN) that was modified by replacing the fragment from NcoI site (CCATGG) to SalI site (GTCGAC) in multicloning site with the sequence "CCATGGGCAGCAGCCATCATCATCATCATCACAGCAGCGGCCTGGTGCCG CGCGGCAGCCATATGCTCGAGCTGGTGCCGCGCGGCAGCGGATCCTAAGT CGAC" (Irie *et al*, 2018). The NavAb mutated DNAs were subcloned between BamHI and SalI sites to add the N-terminal His tag and thrombin cleavage site. The polymerase chain reaction accomplished site-directed mutagenesis using PrimeSTAR® Max DNA Polymerase (Takara Bio). All clones were confirmed by DNA sequencing.

Electrophysiological measurement in insect cells

The recordings were performed using SF-9 cells, (ATCC catalogue number CRL-1711) which were grown in Sf-900™ II medium (Gibco) complemented with 1% 100× Antibiotic-Antimycotic (Fujifilm-Wako) at 27°C. Cells were transfected with target channel-cloned pBiEX-1 vectors and enhanced green fluorescent protein (EGFP)-cloned pBiEX-1 vectors using polyethyleneimine (PEI) reagent (Cosmo bio). PEI was solubilized in distilled water, and 1 mg/mL PEI solution pH was adjusted to 7.0 with NaOH. First, the channel-cloned vector (3.3 μg) was mixed with 1.65 μg of the EGFP-cloned vector in 150 μL of the culture medium. Next, 15 μL 1 mg/mL PEI solution was added, and the mixture was incubated for 10 min before the transfection mixture was gently dropped onto cultured cells. After 24-48 h incubation, the cells were used for electrophysiological measurements.

For reversal potential measurements to determine the relative permeabilities of Li^+ and other cations, the internal pipette solution contained 35 mM NaCl, 115 mM NaF, 10 mM EGTA, and 10 mM HEPES-NaOH (pH 7.4). For the pipette solution was mixed with the acidic solution (35 mM NaCl, 115 mM NaF, 10 mM EGTA, and 10 mM HEPES) and the basic solution (35 mM NaOH, 115 mM NaF, 10 mM EGTA, 10 mM HEPES) to adjust pH 7.4. For the evaluation of cation selectivity, the Li^+ extracellular solution was mixed with the acidic solution (150 mM LiCl, 10 mM HEPES, 10 mM glucose, 2 mM $CaCl_2$) and the basic solution (150 mM LiOH, 10 mM HEPES, 10 mM glucose, 2 mM $CaCl_2$) to adjust pH 7.4. The K^+, $Cs^{+,}$ and Ca^{2+} extracellular solutions were similar, except that all the LiCl and LiOH were replaced by an osmotically

equivalent amount of these cation salts and basic solutions. Cancellation of the capacitance transients and leak subtraction were performed using a programmed P/10 protocol delivered at -140 mV. The bath solution was changed using the Dynaflow® Resolve system. All experiments were conducted at 25 ± 1°C using a whole-cell patch clamp mode with a HEKA EPC 10 amplifier and Patch master data acquisition software (v2x73). Data export was performed using Igor Pro 9.05 and NeuroMatic (v3.0s) (Rothman & Silver, 2018). All sample numbers represent the number of individual cells used for each measurement. Cells with a smaller leak current than 1 nA were used for data collection. When any outliers were encountered, they were excluded if any abnormalities were found in other measurement environments, and they were included if no abnormalities were found. All results are presented as mean ± standard error. The graph data were plotted using Microsoft Excel (v16.87).

Calculation of ion selectivity by the GHK equation

The intracellular and extracellular solutions were arbitrarily set to determine the ion selectivity of each channel. The reversal potential at each concentration was measured by giving a ramp pulse of membrane potential. The applied ramp pulse was set to include the reversal potential. A 10-ms depolarization stimulus was inserted for each measurement to confirm the cell's condition. The permeability ratio of Ca^{2+} (P_{Ca}/P_{Na}) was thus calculated by substituting the obtained reversal potential (E_{rev}) into the expression derived from the GHK equation (Frazier, George, and Jones, 2000):

$$P_{\mathrm{Ca}}/P_{\mathrm{Na}} = \frac{-\left([\mathrm{Na}^+]_{\mathrm{in}} - [\mathrm{Na}^+]_{\mathrm{out}} e^{-E_{\mathrm{rev}}F/RT}\right)\left(1 - e^{-2E_{\mathrm{rev}}F/RT}\right)}{4\left([\mathrm{Ca}^{2+}]_{\mathrm{in}} - [\mathrm{Ca}^{2+}]_{\mathrm{out}} e^{-2E_{\mathrm{rev}}F/RT}\right)\left(1 - e^{-E_{\mathrm{rev}}F/RT}\right)}$$

R, T, F, and E_{rev} are the gas constant, absolute temperature, Faraday constant, and reversal potential, respectively.

The permeation ratio of monovalent cations (P_M/P_{Na}, M represents Li^+, K^+, or Cs^+) was calculated by substituting the obtained reversal potential and P_{Ca}/P_{Na} into the expression derived from the GHK equation (Lopin *et al*, 2012):

$$P_{\mathrm{M}}/P_{\mathrm{Na}} = \left[\frac{-4\left([\mathrm{Ca}^{2+}]_{\mathrm{in}} - [\mathrm{Ca}^{2+}]_{\mathrm{out}} e^{-2E_{\mathrm{rev}}F/RT}\right)\left(1 - e^{-E_{\mathrm{rev}}F/RT}\right)}{\left([\mathrm{Na}^+]_{\mathrm{in}} - [\mathrm{Na}^+]_{\mathrm{out}} e^{-E_{\mathrm{rev}}F/RT}\right)\left(1 - e^{-2E_{\mathrm{rev}}F/RT}\right)} \cdot (P_{\mathrm{Ca}}/P_{\mathrm{Na}}) - 1\right]\left[\frac{\left([\mathrm{Na}^+]_{\mathrm{in}} - [\mathrm{Na}^+]_{\mathrm{out}} e^{-E_{\mathrm{rev}}F/RT}\right)}{\left([\mathrm{M}^+]_{\mathrm{in}} - [\mathrm{M}^+]_{\mathrm{out}} e^{-E_{\mathrm{rev}}F/RT}\right)}\right]$$

Protein expression and purification

Proteins were expressed in the *Escherichia coli* KRX strain (Promega). Cells were grown at 37ºC to an OD_{600} of 0.6, induced with 0.1% rhamnose (Fujifilm-Wako), and grown for 16 h at 20ºC. The cells were suspended in TBS buffer (20 mM Tris-HCl pH 8.0, 150 mM NaCl) and lysed using LAB1000 (SMT Co., LTD.) at 12,000 psi. Low-speed centrifugation removed cell debris (12,000×g, 30 min, 4°C). Membranes were collected by centrifugation (100,000×g, 1 h, 4°C) and solubilized by homogenization in TBS buffer containing 30 mM n-dodecyl-β-D-maltoside (DDM, Anatrace). After centrifugation (40,000×g, 30 min, 4°C), the supernatant was loaded onto a HIS-Select® Cobalt Affinity Gel column (Sigma). The protein bound to the cobalt affinity column was washed with 10 mM imidazole in TBS buffer containing 0.05% lauryl maltose neopentyl glycol (LMNG, Anatrace) instead of DDM. After washing, the protein was eluted with 300 mM imidazole, and the His tag was removed by thrombin digestion (overnight, 4°C). Eluted protein was purified on a Superdex-200 column (Cytiva) in TBS buffer containing 0.05% LMNG.

Crystallization and structural determination

Before crystallization, the purified protein was concentrated to ~10mg ml^{-1} and reconstituted into a bicelle solution (Faham *et al*, 2005), containing a 10% bicelle mixture at 2.8:1 (1,2-dimyristoyl-sn-glycero-3-phosphorylcholine [DMPC, Anatrace]: 3-[(3-cholamidopropyl) dimethylammonio]-2-hydroxypropanesulfonate [CHAPSO, DOJINDO]). The NavAb 10% bicelle was mixed in a 20:1 ratio. Prepared proteins were crystallized by sitting-drop vapor diffusion at 20°C by mixing 300-nl volumes of the protein solution (8–10 mg/ml) and the reservoir solution (9%–11% polyethylene glycol monomethyl ether [PEG MME] 2000, 100 mM sodium chloride, 100 mM magnesium nitrate, 25mM cadmium nitrate and 100 mM Tris-HCl, pH 8.4) with mosquito LCP (STP Labtech). The crystals were grown for 1 to 3 weeks, and after growing, the crystals were transferred into the reservoir solution without cadmium nitrate, which was replaced with the following cryoprotectant solutions. The cryoprotectant solution contains 11% PEG MME 2000, 100 mM Tris-HCl pH 8.4, 2.5 M sodium chloride, 100 mM calcium nitrate, and 20% (v/v) DMSO.

All data were automatically collected at BL41XU and BL45XU of SPring-8 and merged using the ZOO system (Hirata *et al*, 2019). Data were processed by the KAMO system (Yamashita *et al*, 2018) with XDS (BUILT=20220110) (Kabsch, 2010). The dataset of NavAb S178T mutants ($S178T^{NK}$ and $S178T^{NK/TA}$) were obtained from a single crystal, while the data sets of NavAb S178A mutants ($S178A^{NK}$ and

S178A$^{NK/TA}$) and S178G^{NK} were obtained from four, and three crystals, respectively. Analyses of the data with the STARANISO server (Global Phasing Ltd) revealed severely anisotropic crystals. The data sets were therefore ellipsoidally truncated and rescaled to minimize the inclusion of poor diffraction data.

A molecular replacement method with PHASER (McCoy *et al*, 2007) provided the initial phase using the structure of NavAb N49K mutant (pdb code: 8H9W) as the initial model. The final model was constructed in COOT (version 0.9.2) (Emsley *et al*, 2010) and refined in refmac5 (Murshudov *et al*, 1997) and Phenix (version 1.18) (Adams *et al*, 2010). CCP4 package (v.7.0.078) (Winn *et al*, 2011) was used for structural analysis. Data collection and refinement statistics for all crystals are summarized in Supplementary Table 1. All figures were prepared using the program PyMOL 2.5.4 (Schrödinger, LLC, 2015).

Statistics

Electrophysiological data were analysed using Microsoft Excel (v16.87). All results are presented as the mean with standard error (SEM). Student's t-test was used to estimate statistical significance between M181A mutants and their pre-mutants, and $p < 0.05$ was considered statistically significant.

Results

Electrophysiological evaluation of ion selectivity

The SF of NavAb consists of "TLESW", in which the hydroxyl group of the side-chain of Ser178 forms the extracellular entrance of the SF from bulk solution (Figure 1A)(Payandeh *et al*, 2011). When Na^+ accesses the SF from outside, the oxygen atom of the Ser178 side chain is thought to coordinate directly with the ion along with the Glu177 and four water molecules (Corry & Thomas, 2012). We first examined the Li^+ selectivity of Ser178 mutants (named $S178T^{NK}$, $S178V^{NK}$, $S178A^{NK}$, and $S178G^{NK}$) in the NavAb N49K mutant (named N49K). N49K mutation was introduced into all NavAb channels in this study to provide a stable current (Gamal El-Din *et al*, 2013).

Three mutants, $S178T^{NK}$, $S178A^{NK}$, and $S178G^{NK}$, showed current responses in the insect-cell expression system (Figure 1B), $S178V^{NK}$ showed no current. We therefore thought it was impossible to verify larger side-chain mutants than valine. In the Li^+ extracellular solution, the reversal potentials of $S178T^{NK}$, $S178A^{NK}$, and $S178G^{NK}$ differed from that of N49K, indicating that Li^+ selectivity changed by these mutations. For correct evaluation of ion selectivity, it is necessary to accurately measure the reversal potential.

However, it was difficult to measure the reversal potentials of these mutants, whose currents were immediately inactivated. The T206A mutation is known to make NavAb inactivation slower and provides long-lasting currents (Gamal El-Din *et al*, 2019). These T206A mutants of NavAb showed slower inactivation and provided more prolonged currents (Figure 2A). Therefore, we also introduced the T206A mutation to N49K, $S178T^{NK}$, $S178A^{NK,}$ and $S178G^{NK}$ (named N49K/T206A, $S178T^{NK/TA}$, $S178A^{NK/TA}$, and $S178G^{NK/TA}$). Next, the permeation ratio of Li^+ and Na^+ (P_{Li}/P_{Na}) of N49K/T206A, $S178T^{NK/TA}$, $S178A^{NK/TA}$, and $S178G^{NK/TA}$ was evaluated by the reversal potential in a semi bi-ionic environment. The reversal potential of $S178G^{NK/TA}$ was highest among other mutants, indicating $S178G^{NK/TA}$ had the highest Li^+ selectivity (Figure 2B, C). To a lesser extent than $S178G^{NK/TA}$, $S178T^{NK/TA}$ and $S178A^{NK/TA}$ showed comparable positive shifts of reversal potentials relative to N49K/T206A (Figure 2B, C) (Figure 2B, C). P_{Li}/P_{Na} was 2.18 ± 0.14 in $S178G^{NK/TA}$ compared to 0.71 ± 0.02 in the N49K/T206A, 0.96 ± 0.01 in $S178T^{NK/TA}$ and 1.09 ± 0.05 in $S178A^{NK/TA}$ (Table 1). P_{Li}/P_{Na} of $S178G^{NK/TA}$ (2.18 ± 0.14) indicates that $S178G^{NK/TA}$ allows Li^+ to permeate about twice as efficiently as Na^+, which was approximately triple that of N49K/T206A. Next, we also evaluated the selectivity of the other cations. P_K/P_{Na}, P_{Cs}/P_{Na}, and P_{Ca}/P_{Na} remained at low values with little change between N49K/T206A and the other three mutants (Figure 3 and Table 1).

There was no increase in non-selective cation permeability, and only Li^+ selectivity was mainly enhanced in these Ser178 mutants of NavAb.

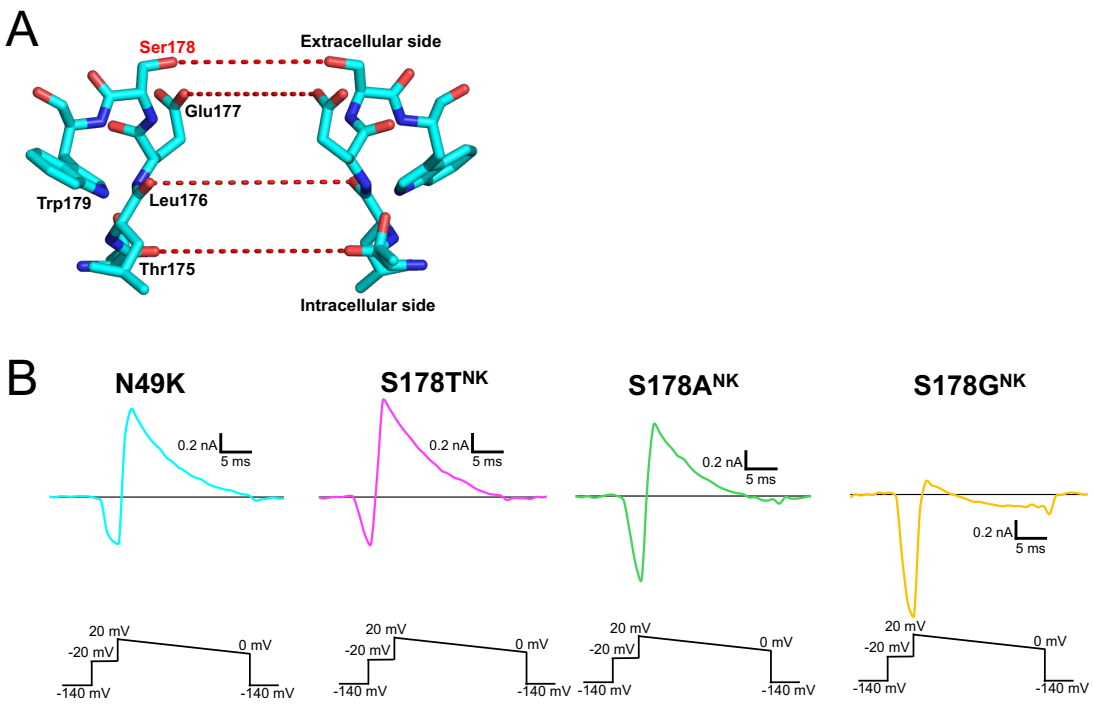

Figure 1. The selectivity filter of NavAb and representative current traces of NavAb N49K, S178T$^{NK/TA}$, S178A^{NK} and S1786G^{NK} mutants

A) Side view of the residues 175-179th constituting the selectivity filter of NavAb-N49K mutant (PDB code: 8H9W). The red dashed lines represent the hydration water exchange sites that ions pass through, formed by the oxygen atoms of the main- and side-chains of the SF. **B)** Recordings of the current responses of NavAb N49K, S178T^{NK}, S178A^{NK}, and S178G^{NK} mutants obtained using the ramp protocol with Li^+ extracellular solution. Currents were generated by the step pulse of -20 mV from -140 mV holding potential, followed by the ramp pulse with different voltage values (shown at the bottom).

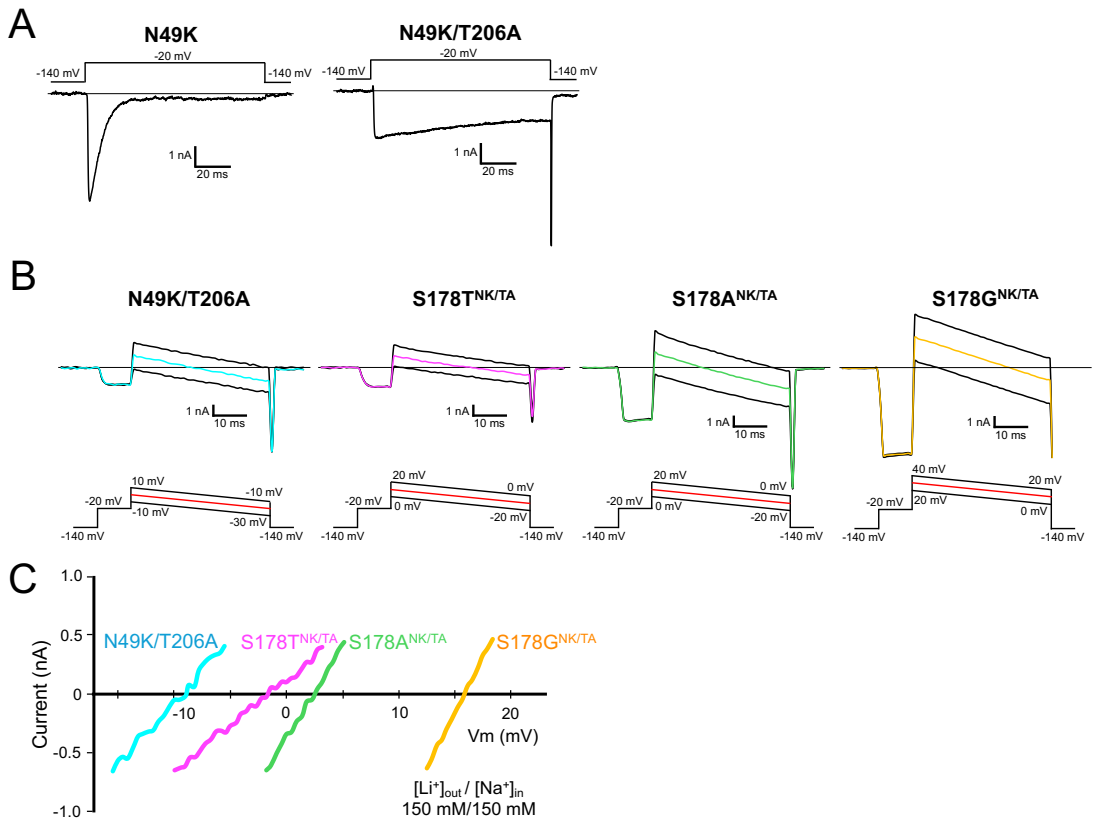

Figure 2. Li^+ selectivity evaluation in NavAb N49K/T206A, $S178T^{NK/TA}$, $S178A^{NK/TA}$, and $S1786G^{NK/TA}$ mutants

A) Whole-cell currents in N49K when a pulse of -20 mV from -140 mV holding potential was given for 100 ms. **B)** Representative current traces of NavAb N49K/T206A, $S178T^{NK/TA}$, $S178A^{NK/TA}$, and $S1786G^{NK/TA}$ mutants were obtained using the ramp protocol. The values of the reversal potential recorded with three different ramp pulses were averaged and used. Currents were measured in 150 mM $[Li^+]_{out}$ and 150 mM $[Na^+]_{in}$. **C)** Current-voltage relationship plots of N49K/T206A, $S178T^{NK/TA}$, $S178A^{NK/TA}$, and $S1786G^{NK/TA}$ generated by the ramp pulses in 150 mM $[Li^+]_{out}$ and 150 mM $[Na^+]_{in}$.

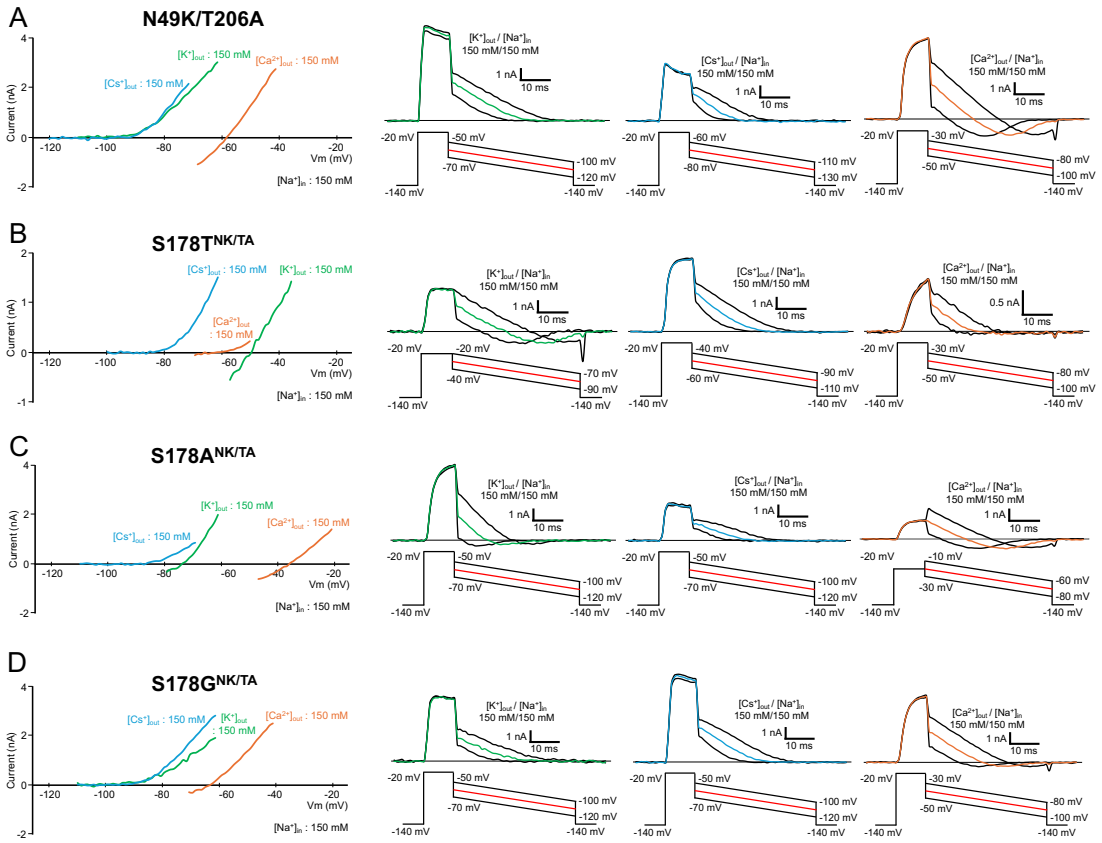

Figure 3. Cation selectivity evaluation in NavAb N49K/T206A, S178T$^{NK/TA}$, S178A$^{NK/TA}$, and S1786G$^{NK/TA}$ mutants

A-D) Current-voltage relationship plots (left) and representative currents (right) used to evaluate the permeability of K^+, Cs^+ and Ca^{2+} relative to that of Na^+ of NavAb N49K/T206A, S178T$^{NK/TA}$, S178A$^{NK/TA}$, and S1786G$^{NK/TA}$ mutants. Currents were measured in 150 mM $[K^+]_{out}$, 150 mM $[Cs^+]_{out}$ and 100 mM $[Ca^{2+}]_{out}$, respectively, and 150 mM $[Na^+]_{in}$. Currents were generated by the step pulse of -20 mV from -140 mV holding potential, followed by the ramp pulses with different voltage values. The time course of the change of membrane potentials are shown at the bottom of the respective current traces.

Table 1. Relative permeability in NavAb N49K/T206A, S178T$^{NK/TA}$, S178A$^{NK/TA}$, and S1786G$^{NK/TA}$ mutants
All values are indicated as SEM.

	P_{Li}/P_{Na}	P_K/P_{Na}	P_{Cs}/P_{Na}	P_{Ca}/P_{Na}
N49K/T206A	0.71 ± 0.02	<0.05*	<0.05*	0.05 ± 0.00
	(n = 10)	(n = 6)	(n = 6)	(n = 8)
S178T$^{NK/TA}$	0.96 ± 0.01	0.13 ± 0.01	<0.05*	<0.05*
	(n = 8)	(n = 4)	(n = 7)	(n = 7)
S178A$^{NK/TA}$	1.09 ± 0.05	0.05 ± 0.00	<0.05*	0.12 ± 0.00
	(n = 11)	(n = 8)	(n = 6)	(n = 6)
S178G$^{NK/TA}$	2.18 ± 0.14	<0.05*	<0.05*	<0.05*
	(n = 11)	(n = 5)	(n = 7)	(n = 9)

*When the reversal potential was below the deactivation potential, P_M/P_{Na} was noted as <0.05 which is the value calculated from the lowest measurable reversal potential in each construct.

Crystal structure of mutants

To reveal the molecular mechanisms of the enhancement of Li^+ selectivity, S178T^{NK}, S178A^{NK}, and S178G^{NK} mutants of NavAb were crystallized, and these structures were determined at approximately 3.0 Å resolution by the same method as used in our previous study of NavAb (Irie *et al*, 2018, 2023). Crystallization was also performed in the mutants containing T206A, but the resolution of these crystals' diffraction patterns deteriorated in all T206A mutants. As with the mutants without T206A, the S178T/T206A mutant showed the best resolution in all T206A mutants, but its resolution was only 3.4 Å (Sup. Table 1). The RMSDs of the Cα carbons of S178T$^{NK/TA}$ mutant to S178T^{NK} were 0.23 Å, and Thr206 is located in the channel lumen, distant from Ser178. T206A is considered to have no effect on the mutation to Ser178, so the structural analysis was performed without T206A.

The electron density fitted well to the mutated side-chain of the 178th residue of all mutants (Figure 4). Their structures resembled the N49K channel (PDB code: 8H9W) (Irie *et al*, 2023). The RMSDs of the Cα carbons of S178T^{NK}, S178A^{NK}, and S178G^{NK} mutants to the N49K were 0.48, 0.52, and 0.46 Å, respectively. The whole structure of each mutant was therefore almost the same as that of the N49K.

The 178th residue is located at the entrance of the ion pathway. Met181 was located on the bulk solution side of the 178th residue, and water molecules were observed beside this vicinity (Figure 4: arrow). In the S178G^{NK} mutant, the highest Li^+-selective mutant, the glycine mutation created a large space around the 178th residue position due to the absence of side chains (Figure 4D). The water molecules in the S178G^{NK} mutant were closest to the entrance of the ion pathway among the other mutants (Figure 4D:

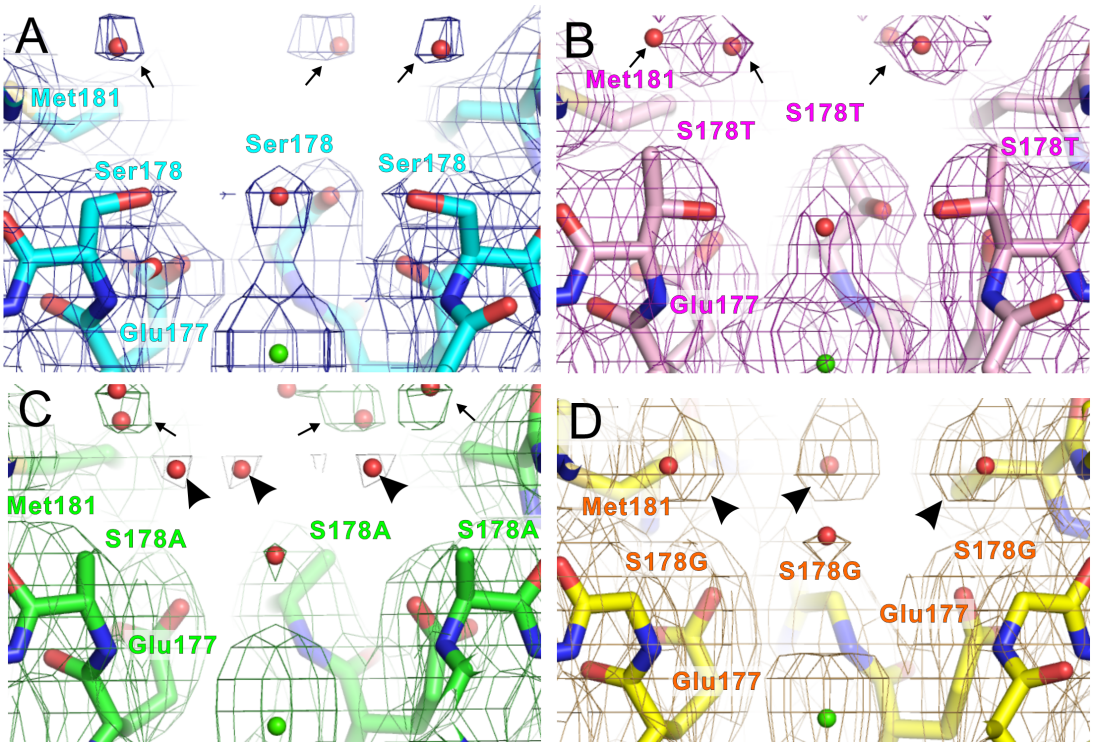

Figure 4. The selectivity filter structure of NavAb N49K, S178T^{NK}, S178A^{NK}, and S178G^{NK} mutants

A-D) Horizontal view of the ion pathway of NavAb N49K, S178T^{NK}, S178A^{NK}, and S1786G^{NK} mutants with the $2F_O - F_C$ electron density map contoured at 1σ, respectively. The carbon atoms of NavAb N49K, S178T^{NK}, S178A^{NK}, and S1786G^{NK} mutants are colored cyan, magenta, green, and yellow, respectively. The electron density of NavAb N49K, S178T^{NK}, S178A^{NK}, and S1786G^{NK} mutants are colored blue, dark magenta, dark green, and orange, respectively. The weak electron density map contoured at 0.5σ are colored gray in NavAb S178A^{NK}. The bulk water molecules are indicated by black arrows. The electron density of water molecules are indicated by black arrowheads.

arrowhead). The S178G mutant showed high Li^+ selectivity, so this difference is thought to contribute to lithium selectivity. Weak electron density was observed in the S178A^{NK}

mutant at a position corresponding to the water molecule near to the entrance of ion pathway in the S178G^{NK} mutant (Figure 4C: arrowhead). Considering that the S178A^{NK} mutant has the second highest Li^+ selectivity, water molecules approaching the channel entrance may be favourable for Li^+ selectivity.

The shape of the ion pathway

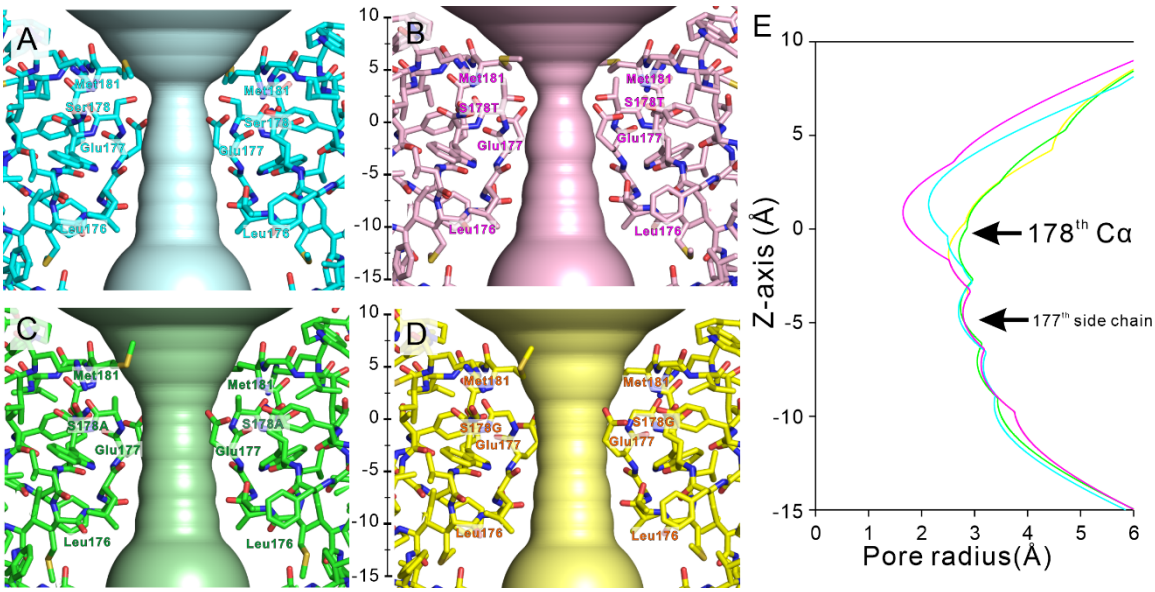

Figure 5. The shapes and radius of the ion pathway of NavAb N49K, S178T^{NK}, S178A^{NK}, and S1786G^{NK} mutants

A-D) Horizontal view of the ion pathway of NavAb N49K, S178T^{NK}, S178A^{NK}, and S1786G^{NK} mutants depicted by program hole. The carbon atoms of NavAb N49K, S178T^{NK}, S178A^{NK}, and S1786G^{NK} mutants are colored cyan, magenta, green, and yellow, respectively. E) The pore radius of NavAb N49K, S178T^{NK}, S178A^{NK}, and S1786G^{NK} mutants. The baseline of the z-axis is the value of z-axis values of the main chain carbonyl oxygen atoms of the 178th residue. The extracellular direction is plotted as plus, and the cytosolic direction as minus.

As the size of the mutated side-chain increased, the radius of the ion pore decreased (Figure 5). In the S178T^{NK} mutants, the mutated side-chain was the narrowest region even within the SF, with a length of less than 2 Å (Figure 5B and E). The wild-type Ser residue forms a similarly narrow region, but the radius of this ion pore is more than 2 Å. In the S178A^{NK} mutant and S178G^{NK}, the shape of the ion pore in this region is more expansive because of the mutated smaller mutant side-chain (Figure 5C and D). These two mutants show improved Li^+ selectivity, so it is possible that the Li^+ selectivity was improved by widening the pore. On the other hand, this is inconsistent with the fact that

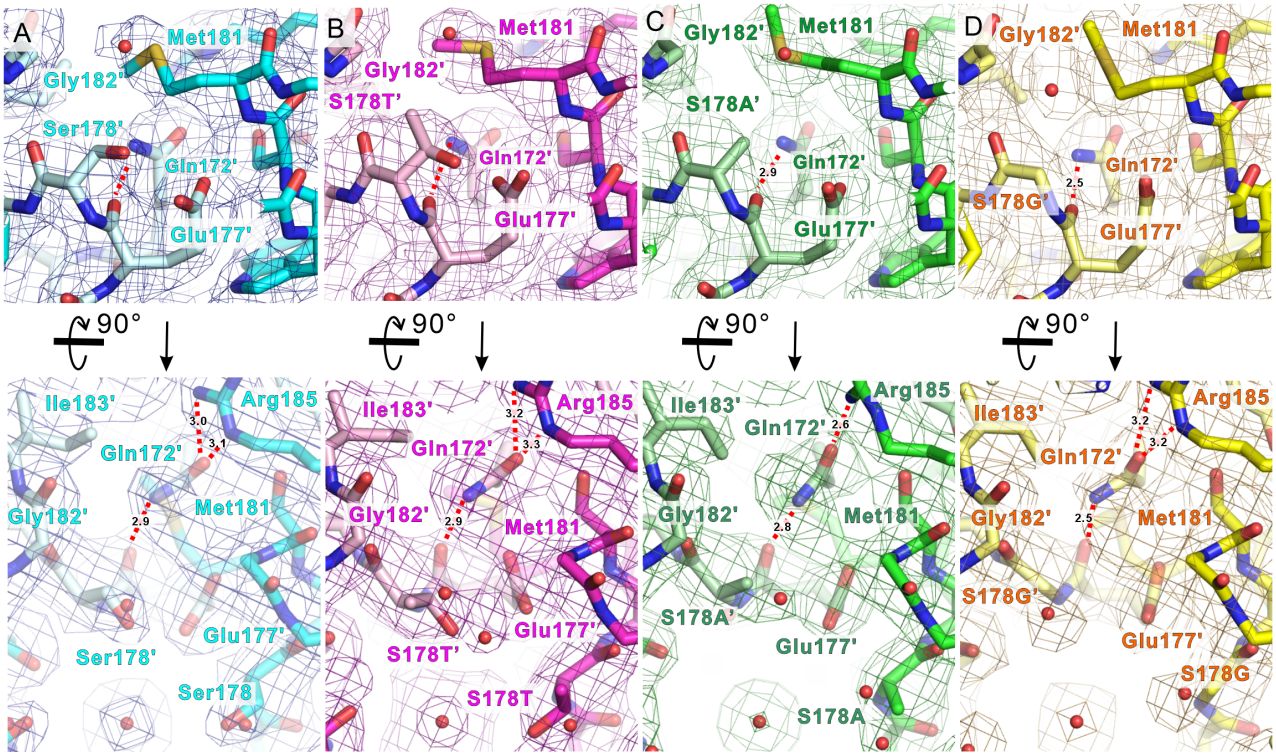

Figure 6. The hydrogen bond network in the backyard of the selectivity filter
A-D) Upper: The horizontal view from the center of the ion pathway of the electron densities and protein structures around Met181 and adjucent subunit's Glu177 and Gln172 of the selectivity filter of NavAb N49K, S178T^{NK}, S178A^{NK}, and S1786G^{NK} mutants, respectively. These figures correspond to the enlarged view of the subunit at the back centre in Figure 4. The $2F_O - F_C$ electron density map contoured at 1σ (blue, dark magenta, dark green, and orange). Lower: The vertical view from the extracellular side of the electron densities and protein structures around Met181, indicating Arg185 interaction was lost in S1786G^{NK}.

S178T^{NK}, which has narrower pores, shows a slight improvement in Li^+ selectivity.

Next, we focused on the residues forming ion pores (Figure 6). The ion pore is formed by the SF sequence of NavAb, TLESW, in which three residues of the "176-LES-178" form the surface of the ion permeation pathway (Figure 5). Met181 was located on the extracellular side of the 178th amino acid residue. In the S178G^{NK} case, the Met181 side chain moved toward the Gln172 side-chain (Figure 6D). Gln172 is located in the backyard of the ion pore, not facing the ion permeation pathway, but its side-chain forms a hydrogen bond with the carbonyl group of the Glu177 main-chain (Figure 6). The side-chain of Glu177, a carboxylate, forms a critical ion recognition site for ion permeation. The side chain of Arg185 forms a hydrogen bond with the oxygen atom of the side-chain of Gln172, and fix the direction of amido group of Gln172 to stabilize

the hydrogen bond between Glu177 main-chain and Gln172 amido group. Similar interactions were observed in the S178T^{NK}, S178A^{NK}, and S178G^{NK} mutants (Figures 6 B-D). The difference of the Met181 observed in S178G^{NK} may therefore be responsible for improving Li^+ selectivity.

Mutational effects of pore-helices on ion permeability

The electron density of water molecules in NavAb S178G^{NK} with the highest Li^+ selectivity was observed at the Ser178 position, the outer edge of the SF. Meanwhile, in S178T^{NK} and S178A^{NK} with enhanced Li^+ selectivity, we observed the electron density of water molecules beside Met181, just before the SF entrance. Accordingly, we hypothesized that Li^+ selectivity increases by the easy blotting of hydrated ions into the vicinity of the SF. The Met181 is at the bottom of the extracellular funnel and narrows the pathway to the SF. The Met181 side chain of S178G^{NK} was especially sunk in the direction of Gln172 (Figure 6D). Therefore, in order to increase Li^+ selectivity by widening the pathway to the SF, M181A mutations were introduced to NavAb N49K/T206A and its Ser178 mutants (N49K/T206A-M181A, S178T$^{NK/TA}$-M181A, S178A$^{NK/TA}$-M181A, and S178G$^{NK/TA}$-M181A). Cells expressing S178T$^{NK/TA}$-M181A showed a little current, and rarely, too weak a current of less than 1 nA to evaluate the reversal potential (Figure 7). Also, cells showing channel activity were few in S178A$^{NK/TA}$-M181A and S178G$^{NK/TA}$-M181A, but a credible reversal potential was obtained. The resulting P_{Li}/P_{Na} were 0.85 ± 0.03 in N49K/T206A-M181A, 1.09 ± 0.04 in S178A$^{NK/TA}$-M181A and 0.99 ± 0.04 in S178G$^{NK/TA}$-M181A, respectively (Table 2). Li^+ selectivity increased significantly in N49K/T206A-M181A ($p < 0.01$) and decreased significantly in S178G$^{NK/TA}$-M181A ($p < 0.01$) compared with their pre-mutants. In S178A$^{NK/TA}$-M181A, Li^+ selectivity was almost unchanged. In other words, the P_{Li}/P_{Na} of those mutants approached 1 , which means non-selective for Li^+ and Na^+. P_{Ca}/P_{Na} significantly increased in all mutants compared with their pre-mutants. The M181A mutation is indicated by these results to have caused a loss of cation selectivity in these mutant channels. Met181 was thus shown to support the function of the SF and to achieve Li^+ selectivity in NavAb.

The pore-loop between S5 and S6 comprises P1-helix, the SF, and P2-helix in the order from the N-terminal side. These pore-helices do not face the ion pore and provide a robust backbone for the SF. Especially, P1-helix forms an extracellular funnel shape. Referring to the crystal structure of NavAb, Met181 is at the edge of the P2-helix, the boundary between the SF and extracellular funnel, and its side-chain extends its toe toward Gln172 at the P1-helix of the neighboring subunit. In the interaction network

around the SF, the side-chain of Gln172 in particular forms hydrogen bonds with the main-chain carbonyl of Glu177. The Glu177 of NavAb forms a strong ion recognition site and critically affects ion permeability (Payandeh *et al*, 2011). We therefore predicted that Met181 of NavAb controls ion selectivity via Gln172, which interacts directly with Glu177. Then, the Gln172 of NavAb N49K/T206A and S178G$^{NK/TA}$ were mutated to evaluate its role in regulating Li^+ selectivity. The asparagine side-chain is shorter than that of glutamine by one methyl group, so the Q172N mutation was expected to weaken or lose the hydrogen bond networks between Glu177 and Arg185. Unexpectedly, neither NavAb Q172N mutant conducted any current. This fatal loss of function due to a small difference in side-chain length suggested the critical role of Gln172 in ion permeability and stability of the SF of NavAb.

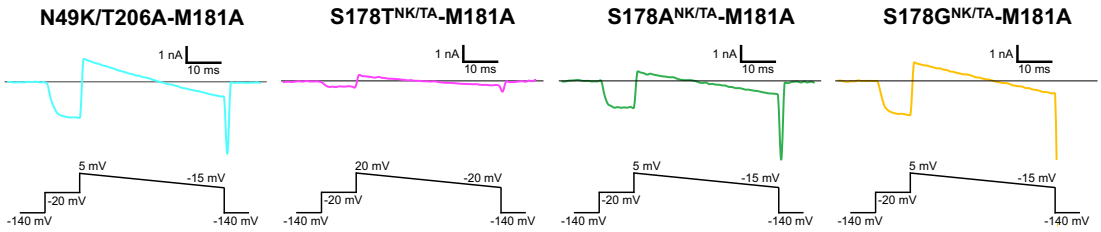

Figure 7. Current traces of NavAb Met181 mutants and Gln172 mutants
A) Representative current traces of NavAb N49K/T206A-M181A, S178T$^{NK/TA}$-M181A, S178A$^{NK/TA}$-M181A, and S178G$^{NK/TA}$-M181A mutants obtained using the ramp protocol. Currents were measured in 150 mM $[Li^+]_{out}$ and 150 mM $[Na^+]_{in}$.

Table 2. Relative permeability in NavAb Met181 mutants
All values are indicated as SEM. The p-values represent the results of Student's t test with the M181A pre-mutants (N49K/T206A, S178A$^{NK/TA}$ and S178G$^{NK/TA}$).

	P_{Li}/P_{Na}			P_K/P_{Na}			P_{Cs}/P_{Na}		P_{Ca}/P_{Na}		
N49K/T206A-M181A	0.84	± 0.03	$p < 0.01$	<0.05*	± 0.03	NS	<0.01*	$p < 0.01$	0.36	± 0.02	$p < 0.01$
	(n = 8)			(n = 3)			(n = 6)		(n = 4)		
S178A$^{NK/TA}$-M181A	1.09	± 0.04	NS	0.09	± 0.01	$p < 0.01$	<0.05*	NS	0.41	± 0.05	$p < 0.01$
	(n = 7)			(n = 5)			(n = 5)		(n = 7)		
S178G$^{NK/TA}$-M181A	0.99	± 0.04	$p < 0.01$	<0.05*	± 0.01	NS	<0.05*	NS	0.47	± 0.05	$p < 0.01$
	(n =3)			(n = 3)			(n = 3)		(n = 4)		

*When the reversal potential was below the deactivation potential, P_M/P_{Na} was noted as <0.05 which is the value calculated from the lowest measurable reversal potential in each construct.

Discussion

Ion selectivity analyses using modified BacNavs have been reported, but Li^+ selectivity in all mutants was almost unchanged from that of wild-types (P_{Li}/P_{Na} = 0.6~0.8 in wild-types and their mutants) (DeCaen *et al*, 2014; Finol-Urdaneta *et al*, 2014; Naylor *et al*, 2016). In this study, we found that the Ser178 mutations of NavAb enhance Li^+ selectivity. Following the nomenclature of artificial bacterial channels (Yue *et al*, 2002; Tang *et al*, 2014), NavAb mutants with S178G mutation are henceforth collectively referred to as "LivAb" based on their high Li^+ selectivity ($S178G^{NK}$ and $S178G^{NK/TA}$ were named $LivAb^{NK}$ and $LivAb^{NK/TA}$, respectively). Also, in this study we investigated the molecular basis of Li^+ permeation from the crystal structure of each mutant. Li^+ selectivity increased by the loss of the hydroxyl group or the decline of the side-chain size at the 178th residue of NavAb. As described later, it suggests that the lower times of the hydration water exchanges and the wider entrance of the SF are suitable for Li^+ permeation in Nav.

Hydration water exchanges have been shown to be crucial for ion permeation in Navs (Ahern *et al*, 2016). Referring to the crystal structure of NavAb, the oxygen atoms in the main- and side-chains in the SF form four hydration water exchange sites (Figure 1A) (Payandeh *et al*, 2011). Na^+ in the bulk solution is fully hydrated with bulk water molecules and exchanges hydration water one after the other during Brownian diffusion. When Na^+ approaches the outer edge of the SF in BacNavs, it first interacts with proteins via water molecules (Naylor *et al*, 2016). In the case of NavAb, entering into the SF requires the Na^+ to release two hydration waters, which are replaced by the oxygen atoms of the side-chains of Ser178 and Glu177 (Corry & Thomas, 2012). These oxygen atoms coordinate to Na^+ instead of the hydration water as negative dipolar. Na^+ entering the ion pore by hydration with the side-chain of Glu177 passes through the following hydration water exchange sites formed by the oxygen atoms of the main-chain carbonyls of Leu176 and Thr175, and then enters the central cavity (Payandeh *et al*, 2011; Chakrabarti *et al*, 2013). These hydration water exchange schemes allow Na^+ to permeate the SF step by step at nearly the rate of free diffusion (Hille, 2001). The diameter of the SF in Navs is sufficiently wide that two to three Na^+ ions are accommodated in the SF and permeate in a hydrated or partially dehydrated state (Chakrabarti *et al*, 2013; McCusker *et al*, 2012; Payandeh *et al*, 2011; Shaya *et al*, 2014; Tsai *et al*, 2013; Ulmschneider *et al*, 2013). In other words, changes in the number, location, and timing of hydration water exchanges in the SF will significantly affect the permeation efficiency of ions with different properties.

Hydration water exchange is one of the rate-limiting steps of ion transfer in the

solution. Each ion has a unique value in the exchange rate of hydration water, and ions with a slower exchange rate move more slowly in an aqueous solution (Hille, 2001). Na^+ and Li^+ are monovalent and single-atom cations, and the ionic radius of Li^+ (0.60 Å) is smaller than that of Na^+ (0.95Å). Owing to the small radius, Li^+ has a stronger electrical interaction with negative dipolar of water molecules than Na^+, resulting in a slower rate of hydration water exchange. In the SF, the hydroxyl groups take the place of water molecules, and ions pass through the hydration water exchange sites stepwise with hydration water exchanges. Hence, the more hydration water exchange sites formed by hydroxyl groups in the SF, the slower the rate of permeation of Li^+ with strong interaction force and the lower its permeability. In this study, 178th residues of hydroxyl groups were lost in $S178A^{NK/TA}$ and $S178G^{NK/TA}$ ($LivAb^{NK/TA}$) compared with N49K/T206A of NavAb (Figure 8). This loss of one of the hydration water exchange sites may have increased the permeability of Li^+, which has a slower hydration exchange rate than Na^+.

Next, we consider why the wider entrance of the SF is advantageous for Li^+ permeation. One of the leading reasons is that widening the entrance exposes the most potent ion-recognition sites directly to the extracellular solution. As mentioned earlier, ions need to be fully or partially dehydrated to pass through the SF. To do so, the interaction energy between the ion and the oxygen atoms in the SF must exceed the dehydration energy of ion. The strength of the interaction energy depends inversely on the sum of the radii of two particles , so ion with smaller radius is more dehydratable when approaching a partner particle (Hille, 2001). Following this nature rule, Eisenman experimentally and theoretically classified the selectivity of five alkali metal cations, including Li^+ and Na^+, into eleven broad categories (Eisenman, 1962). In the present study, the ion selectivity of NavAb $S178G^{NK/TA}$ ($LivAb^{NK/TA}$) was consistent with the XI ($Li^+ > Na^+ > K^+$, Cs^+) in Eisenman sequence. This XI order is the case where the electric force interacting with cations is the strongest. The most potent ion-recognition sites of NavAb comprise the Glu177 side-chain, the only negatively charged part among the SF (TLESW) (Payandeh *et al*, 2011). The Glu177 of NavAb and corresponding residues of eukaryotic Navs and Cavs is known to bind to cations along with water molecules and facilitate ion permeation (Boiteux *et al*, 2014; Chakrabarti *et al*, 2013; Favre *et al*, 1996; Ke *et al*, 2014; Lipkind & Fozzard, 2000; Xia *et al*, 2013). The side-chain of the 178th residue is located between the

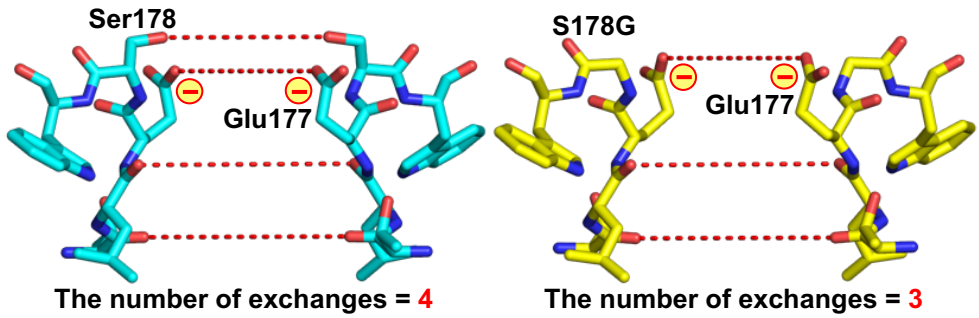

Figure 8. The selectivity filter of NavAb N49K and S178G$^{NK/TA}$ (LivAb$^{NK/TA}$) mutants

Side view of the residues 175-179th constituting the SF of N49K (left, PDB code 8H9W) and S178G$^{NK/TA}$ (LivAb$^{NK/TA}$) (right, PDB code 9UC3). The red dashed lines represent the hydration water exchange sites which ions pass through, formed by the oxygen atoms of the main and side chains of the SF.

Glu177 side-chain and the bulk extracellular region, so a smaller side-chain of the 178th residue would directly expose the most potent ion recognition site to the extracellular solution. The most expansive vestibule of the SF in S178G$^{NK/TA}$ (LivAb$^{NK/TA}$) allows ions to get close to the exposed Glu177 directly without dehydration. This is advantageous for interaction with Li^+, which has a smaller ionic radius in addition to a strong positive charge than Na^+. Interactions with Glu177 in closer proximity was thought to facilitate the dehydration and permeation of Li^+, reversing the permeability Li^+ and Na^+. The water molecules at the 178th residue position in the crystal structure of S178G$^{NK/TA}$ (LivAb$^{NK/TA}$) support the explanation that hydrated ions in an external solution can enter near Glu177.

With regard to this Li^+ selectivity enhancement in NavAb based on exposed negative chaeges is thought to be partly similar in principle to the artificial Ca^{2+} selectivity in some BacNav mutants (Yue *et al*, 2002; DeCaen *et al*, 2014; Tang *et al*, 2014). In those artificial Cavs, Ca^{2+} selectivity is enhanced by adding negative charges to the SF. Here, we should focus on why the NavAb-S178G$^{NK/TA}$ mutant retained low Ca^{2+} selectivity, with $P_{Ca}/P_{Na} < 0.01$, while boosting Li^+ selectivity. We previously reported the only identified prokaryotic Cav, CavMr (Irie, 2021; Shimomura *et al*, 2020). CavMr functions as a homo-tetramer like prokaryotic Navs, and the SF sequence of CavMr is "TLEGW", the same as that of S178G$^{NK/TA}$ (LivAb$^{NK/TA}$). The glycine residue in the SF (TLEGW) of CavMr plays a key role in Ca^{2+} selectivity, and a single-point mutation of its glycine to serine decreases P_{Ca}/P_{Na} about 18-fold. In contrast, in this study, the S178G mutation in NavAb affected only Li^+ selectivity, not Ca^{2+} selectivity. However, all NavAb M181A mutants changed to non-selective channels

with moderate Li^+ permeability equivalent to Na^+ and approximately 10-fold Ca^{2+} selectivity. This result suggest that the Met181 in NavAb sorts monovalent and divalent cations (Li^+ v.s. Ca^{2+} in this case). The position of Met181 in CavMr is aspartate (Shimomura *et al*, 2020), and the same for artificial Cavs (CachBac and CavAb) (Yue *et al*, 2002; Tang *et al*, 2014), so this aspartate side-chain has been considered to affect cation permeability by electric interaction. However, if only the electric repulsion between cations and the hydrophobic side-chain of Met181 is essential for ion selectivity, Li^+ should also be excluded by its strong positive charges at the entrance of the SF, as well as Ca^{2+}. In other words, factors other than electric force are thought to be involved in the regulation of ion selectivity by the Met181 in NavAb.

Around the SF, the extensive interactions are formed by several residues within the same subunit or between neighboring subunits (Payandeh *et al*, 2011). As for the crystal structure of NavAb, it had been known that Met181 and Gln172 at the pore-helices also form part of the network, but their roles had only rarely been experimentally evaluated. In this study, the small number of cells showing activity and low currents in NavAb M181A mutants with non-selectivity proposed the idea that Met181 regulates ion selectivity by the SF stabilization. In addition, the Q172N mutation abolished the channel currents, suggesting that Gln172 interacting with the main-chain carbonyl of Glu177 is critically responsible for ensuring ion permeation via Glu177. To better understand the molecular basis of Li^+ selectivity, detailed analyses of these extensive interactions are required, especially those between the SF and pore-helices.

In summary, the present study suggested the mechanisms of enhanced Li^+ selectivity in NavAb. Differences in the width of the SF entrance and each ionic property, such as electric interaction force, hydration water exchange rate, ionic radii and valences, determine the selectivity of Na^+ and Li^+. Also, the SF stabilization by the extensive interactions with the extracellular funnel and pore-helices supports this ion permeation in the ion pore. These discoveries of Li^+ permeation mechanisms in Navs and the creation of LivAb, a novel “Li channel”, are thought to provide direction for drug development targeting various neurological disorders.

Data availability

The data that support this study are available from the corresponding authors upon request. The structural data generated in this study have been deposited in the Protein Data Bank under accession codes 8H9W (NavAb N49K mutant in calcium), 9UC1 (NavAb S178T^{NK} mutant), 9UC2 (NavAb S178A^{NK} mutant), 9UC3 (NavAb S178G^{NK} mutant [LivAb^{NK}]), and 9UC4 (NavAb S178T$^{NK/TA}$ mutant). The structure of the NavAb N49K mutant for the initial model of molecular replacement was available in the Protein Data Bank under accession code 8H9W.

Author contributions

Yuki K. Maeda: Conceptualization; Resources; Data curation; Formal analysis; Validation; Investigation; Writing - original draft, Writing - review and editing;
Kentaro Kojima: Data curation
Tomoe Y. Nakamura-Nishitani: Writing - review and editing
Toru Nakatsu: Funding acquisition; Writing - review and editing
Katsumasa Irie: Conceptualization; Funding acquisition; Resources; Data curation; Software; Formal analysis; Supervision; Validation; Investigation; Visualization; Writing - original draft; Project administration; Writing - review and editing

Disclosure and competing interests statement

The authors declare no competing interests.

Acknowledgements

The synchrotron radiation experiments were performed at BL41XU and BL32XU in SPring-8 with the approval of the Japan Synchrotron Radiation Research Institute (JASRI) (Proposal numbers 2016B2721, 2017B2735, and 2018B2710). We thank the beamline staff for their excellent facilities and support. This research was partially supported by Platform Project for Supporting Drug Discovery and Life Science Research (Basis for Supporting Innovative Drug Discovery and Life Science Research [BINDS]) from AMED under Grant Numbers JP22ama121001 and JP23ama121001. This work was supported by Grants-in-Aid for Scientific Research (17K17795, 20K09193, and 24K02168) and SEI Group CSR Foundation, Takeda Science Foundation, Institute for Fermentation, and the Salt Science Research Foundation.

Supplementary Table 1. Data collection and refinement statistics.

	S178T^{NK}	S178A^{NK}	S178G^{NK} (LivAb^{NK})	S178T$^{NK/TA}$	S178A$^{NK/TA}$
Wavelength(Å)			1.00		
PDB entry	9UC1	9UC2	9UC3	9UC4	-
Resolution range	45 - 2.6	45 - 2.9	44 - 3.0	45 - 3.4	45 - 4.1
	(2.7 - 2.6)	(3.0 - 2.9)	(3.1 - 3.0)	(3.5 - 3.4)	(4.2 - 4.1)
Space group			*I* 4 2 2		
Unit cell	128.0	126.6	128.1	128.7	127.4
	128.0	126.6	128.1	128.7	127.4
	200.3	201.5	200.4	202.0	203.2
	90	90	90	90	90
	90	90	90	90	90
	90	90	90	90	90
Total reflections	377716	1921436	1186605	302043	511269
	(32294)	(173268)	(111060)	(31081)	(33308)
Unique reflections	25937	18554	17093	12030	6866
	(938)	(824)	(748)	(527)	(381)
Multiplicity	14.6	103.6	69.4	25.1	74.5
	(12.8)	(95.1)	(67.0)	(26.9)	(50.0)
Completeness (%)	86.69	90.19	90.68	92.10	94.03
	(37.08)	(45.23)	(45.11)	(45.51)	(57.12)
Mean I/sigma(I)	27.90	24.02	21.30	10.66	19.85
	(1.32)	(1.55)	(1.20)	(1.41)	(2.66)
R_{merge}	0.051	0.343	0.160	0.677	0.349
	(1.863)	(5.400)	(6.727)	(7.837)	(2.766)
R_{pim}	0.014	0.037	0.022	0.142	0.039
	(0.537)	(0.555)	(0.823)	(1.534)	(0.392)
CC1/2	1	0.997	0.997	0.996	1
	(0.765)	(0.832)	(0.806)	(0.743)	(0.864)
R_{work}	0.259	0.248	0.273	0.279	-
	(0.262)	(0.296)	(0.372)	(0.300)	

R_{free}	0.274 (0.296)	0.282 (0.307)	0.300 (0.467)	0.299 (0.363)	-
Number of non-hydrogen atoms	2345	2345	2276	2343	-
macromolecules	1871	1869	1804	1869	-
ligands	449	449	449	449	-
solvent	25	27	23	25	-
Protein residues	229	229	220	229	-
RMS(bonds)	0.004	0.014	0.013	0.004	-
RMS(angles)	0.82	1.77	1.54	0.74	-
Ramachandran favored (%)	98.24	98.24	98.15	99.12	-
Ramachandran allowed (%)	1.76	1.76	1.85	0.88	-
Ramachandran outliers (%)	0.00	0.00	0.00	0.00	-
Rotamer outliers (%)	0.00	0.00	0.00	0.00	-
Clash score	15.73	17.35	14.48	11.30	-
Average B-factor	91.18	80.37	91.37	112.20	-
macromolecules	88.64	78.44	89.96	110.18	-
ligands	103.54	90.45	99.29	122.13	-
solvent	59.47	46.79	47.04	85.41	-

References

Abriel H & Kass RS (2005) Regulation of the Voltage-Gated Cardiac Sodium Channel Nav1.5 by Interacting Proteins. *Trends in Cardiovascular Medicine* 15: 35–40

Adams PD, Afonine PV, Bunkóczi G, Chen VB, Davis IW, Echols N, Headd JJ, Hung L-W, Kapral GJ, Grosse-Kunstleve RW, *et al* (2010) *PHENIX* : a comprehensive Python-based system for macromolecular structure solution. *Acta Crystallogr D Biol Crystallogr* 66: 213–221

Agwa AJ, Peigneur S, Chow CY, Lawrence N, Craik DJ, Tytgat J, King GF, Henriques ST & Schroeder CI (2018) Gating modifier toxins isolated from spider venom: Modulation of voltage-gated sodium channels and the role of lipid membranes. *Journal of Biological Chemistry* 293: 9041–9052

Ahern CA, Payandeh J, Bosmans F & Chanda B (2016) The hitchhiker's guide to the voltage-gated sodium channel galaxy. *Journal of General Physiology* 147: 1–24

Bagal SK, Marron BE, Owen RM, Storer RI & Swain NA (2015) Voltage gated sodium channels as drug discovery targets. *Channels* 9: 360–366

Boiteux C, Vorobyov I & Allen TW (2014) Ion conduction and conformational flexibility of a bacterial voltage-gated sodium channel. *Proc Natl Acad Sci USA* 111: 3454–3459

Bortolozzi A, Fico G, Berk M, Solmi M, Fornaro M, Quevedo J, Zarate CA, Kessing LV, Vieta E & Carvalho AF (2024) New Advances in the Pharmacology and Toxicology of Lithium: A Neurobiologically Oriented Overview. *Pharmacol Rev* 76: 323–357

Cade JFJ (1949) LITHIUM SALTS IN THE TREATMENT OF PSYCHOTIC EXCITEMENT. *Medical Journal of Australia* 2: 349–352

Campbell DT (1976) Ionic selectivity of the sodium channel of frog skeletal muscle. *The Journal of general physiology* 67: 295–307

Carvalho AF, Quevedo J, McIntyre RS, Soeiro-de-Souza MG, Fountoulakis KN, Berk M, Hyphantis TN & Vieta E (2015) Treatment Implications of Predominant Polarity and the Polarity Index: A Comprehensive Review. *International Journal of Neuropsychopharmacology* 18: pyu079–pyu079

Catterall WA (2000) From ionic currents to molecular mechanisms: the structure and function of voltage-gated sodium channels. *Neuron* 26: 13–25

Catterall WA (2017) Forty Years of Sodium Channels: Structure, Function, Pharmacology, and Epilepsy. *Neurochem Res* 42: 2495–2504

Catterall WA (2023) Voltage gated sodium and calcium channels: Discovery, structure, function, and Pharmacology. *Channels* 17: 2281714

Catterall WA, Cestèle S, Yarov-Yarovoy V, Yu FH, Konoki K & Scheuer T (2007) Voltage-gated ion channels and gating modifier toxins. *Toxicon* 49: 124–141

Catterall WA & Zheng N (2015) Deciphering voltage-gated Na+ and Ca2+ channels by studying prokaryotic ancestors. *Trends in Biochemical Sciences* 40: 526–534

Chakrabarti N, Ing C, Payandeh J, Zheng N, Catterall WA & Pomès R (2013) Catalysis of Na^+ permeation in the bacterial sodium channel Na_V Ab. *Proc Natl Acad Sci USA* 110: 11331–11336

Chevalier N, Guillou P, Viguié C, Fini J-B, Sachs LM, Michel-Caillet C & Mhaouty-Kodja S (2024) Lithium and endocrine disruption: A concern for human health? *Environment International*: 108861

Corry B & Thomas M (2012) Mechanism of Ion Permeation and Selectivity in a Voltage Gated Sodium Channel. *J Am Chem Soc* 134: 1840–1846

De Lera Ruiz M & Kraus RL (2015) Voltage-Gated Sodium Channels: Structure, Function, Pharmacology, and Clinical Indications. *J Med Chem* 58: 7093–7118

DeCaen PG, Takahashi Y, Krulwich TA, Ito M & Clapham DE (2014) Ionic selectivity and thermal adaptations within the voltage-gated sodium channel family of alkaliphilic Bacillus. *eLife* 3: e04387

Eisenman G (1962) Cation Selective Glass Electrodes and their Mode of Operation. *Biophysical Journal* 2: 259–323

Emsley P, Lohkamp B, Scott WG & Cowtan K (2010) Features and development of *Coot*. *Acta Crystallogr D Biol Crystallogr* 66: 486–501

England S & De Groot MJ (2009) Subtype-selective targeting of voltage-gated sodium channels. *British J Pharmacology* 158: 1413–1425

Faham S, Boulting GL, Massey EA, Yohannan S, Yang D & Bowie JU (2005) Crystallization of bacteriorhodopsin from bicelle formulations at room temperature. *Protein Science* 14: 836–840

Favre I, Moczydlowski E & Schild L (1996) On the structural basis for ionic selectivity among Na+, K+, and Ca2+ in the voltage-gated sodium channel. *Biophysical Journal* 71: 3110–3125

Finol-Urdaneta RK, Wang Y, Al-Sabi A, Zhao C, Noskov SY & French RJ (2014) Sodium channel selectivity and conduction: Prokaryotes have devised their own molecular strategy. *Journal of General Physiology* 143: 157–171

Fountoulakis KN, Grunze H, Vieta E, Young A, Yatham L, Blier P, Kasper S & Moeller HJ (2016) The International College of Neuro-Psychopharmacology (CINP) treatment guidelines for Bipolar disorder in adults (CINP-BD-2017), part 3: The clinical guidelines. *IJNPPY*: pyw109

Frazier CJ, George EG & Jones SW (2000) Apparent Change in Ion Selectivity Caused by Changes in Intracellular K+ during Whole-Cell Recording. *Biophysical Journal* 78:

1872–1880
Gamal El-Din TM, Lenaeus MJ, Ramanadane K, Zheng N & Catterall WA (2019) Molecular dissection of multiphase inactivation of the bacterial sodium channel NaVAb. *Journal of General Physiology* 151: 174–185
Gamal El-Din TM, Martinez GQ, Payandeh J, Scheuer T & Catterall WA (2013) A gating charge interaction required for late slow inactivation of the bacterial sodium channel NavAb. *Journal of General Physiology* 142: 181–190
Hart DA (2024) Lithium Ions as Modulators of Complex Biological Processes: The Conundrum of Multiple Targets, Responsiveness and Non-Responsiveness, and the Potential to Prevent or Correct Dysregulation of Systems during Aging and in Disease. *Biomolecules* 14: 905
Hille B (1972) The Permeability of the Sodium Channel to Metal Cations in Myelinated Nerve. *The Journal of General Physiology* 59: 637–658
Hille B (2001) Ion Channels of Excitable Membranes
Hirata K, Yamashita K, Ueno G, Kawano Y, Hasegawa K, Kumasaka T & Yamamoto M (2019) *ZOO* : an automatic data-collection system for high-throughput structure analysis in protein microcrystallography. *Acta Crystallogr D Struct Biol* 75: 138–150
Hodgikin AL & Huxley AF (1952) A quantitative description of membrane current and its application to conduction and excitation in nerve. *J Physiol* 117: 500–544
Irie K (2021) The insights into calcium ion selectivity provided by ancestral prokaryotic ion channels. *BIOPHYSICS* 18: 274–283
Irie K, Haga Y, Shimomura T & Fujiyoshi Y (2018) Optimized expression and purification of NavAb provide the structural insight into the voltage dependence. *FEBS Lett* 592: 274–283
Irie K, Oda Y, Sumikama T, Oshima A & Fujiyoshi Y (2023) The structural basis of the divalent cation blocking on tetrameric cation channel In Review
Jiang D, Shi H, Tonggu L, Gamal El-Din TM, Lenaeus MJ, Zhao Y, Yoshioka C, Zheng N & Catterall WA (2020) Structure of the Cardiac Sodium Channel. *Cell* 180: 122-134.e10
Jurkat-Rott K, Holzherr B, Fauler M & Lehmann-Horn F (2010) Sodium channelopathies of skeletal muscle result from gain or loss of function. *Pflugers Arch - Eur J Physiol* 460: 239–248
Kabsch W (2010) *XDS*. *Acta Crystallogr D Biol Crystallogr* 66: 125–132
Ke S, Timin EN & Stary-Weinzinger A (2014) Different Inward and Outward Conduction Mechanisms in NaVMs Suggested by Molecular Dynamics Simulations. *PLoS Comput Biol* 10: e1003746

Liebeskind BJ, Hillis DM & Zakon HH (2013) Independent acquisition of sodium selectivity in bacterial and animal sodium channels. *Current Biology* 23: R948–R949

Lipkind GM & Fozzard HA (2000) KcsA Crystal Structure as Framework for a Molecular Model of the Na^+ Channel Pore. *Biochemistry* 39: 8161–8170

Lopin KV, Thévenod F, Page JC & Jones SW (2012) Cd^{2+} Block and Permeation of Ca_V 3.1 (α1G) T-Type Calcium Channels: Candidate Mechanism for Cd^{2+} Influx. *Mol Pharmacol* 82: 1183–1193

Lu Z, Jiang Y-P, Wu C-YC, Ballou LM, Liu S, Carpenter ES, Rosen MR, Cohen IS & Lin RZ (2013) Increased Persistent Sodium Current Due to Decreased PI3K Signaling Contributes to QT Prolongation in the Diabetic Heart. *Diabetes* 62: 4257–4265

Malhi GS, Bassett D, Boyce P, Bryant R, Fitzgerald PB, Fritz K, Hopwood M, Lyndon B, Mulder R, Murray G, *et al* (2015) Royal Australian and New Zealand College of Psychiatrists clinical practice guidelines for mood disorders. *Aust N Z J Psychiatry* 49: 1087–1206

McCoy AJ, Grosse-Kunstleve RW, Adams PD, Winn MD, Storoni LC & Read RJ (2007) *Phaser* crystallographic software. *J Appl Crystallogr* 40: 658–674

McCusker EC, Bagnéris C, Naylor CE, Cole AR, D'Avanzo N, Nichols CG & Wallace BA (2012) Structure of a bacterial voltage-gated sodium channel pore reveals mechanisms of opening and closing. *Nat Commun* 3: 1102

Murshudov GN, Vagin AA & Dodson EJ (1997) Refinement of Macromolecular Structures by the Maximum-Likelihood Method. *Acta Crystallogr D Biol Crystallogr* 53: 240–255

Naylor CE, Bagnéris C, DeCaen PG, Sula A, Scaglione A, Clapham DE & Wallace B (2016) Molecular basis of ion permeability in a voltage-gated sodium channel. *The EMBO Journal* 35: 820–830

Nestsiarovich A, Gaudiot CES, Baldessarini RJ, Vieta E, Zhu Y & Tohen M (2022) Preventing new episodes of bipolar disorder in adults: Systematic review and meta-analysis of randomized controlled trials. *European Neuropsychopharmacology* 54: 75–89

Pappone PA (1980) Voltage-clamp experiments in normal and denervated mammalian skeletal muscle fibres. *The Journal of Physiology* 306: 377–410

Payandeh J, Scheuer T, Zheng N & Catterall WA (2011) The crystal structure of a voltage-gated sodium channel. *Nature* 475: 353–358

Rothman JS & Silver RA (2018) NeuroMatic: An Integrated Open-Source Software Toolkit for Acquisition, Analysis and Simulation of Electrophysiological Data. *Front Neuroinform* 12: 14

Rusina E, Simonti M, Duprat F, Cestèle S & Mantegazza M (2024) Voltage-gated sodium channels in genetic epilepsy: up and down of excitability. *Journal of Neurochemistry* 168: 3872–3890

Schlief T, Schönherr R, Imoto K & Heinemann SH (1996) Pore properties of rat brain II sodium channels mutated in the selectivity filter domain. *European Biophysics Journal* 25: 75–91

Schrauzer GN (2002) Lithium: Occurrence, Dietary Intakes, Nutritional Essentiality. *Journal of the American College of Nutrition* 21: 14–21

Schrödinger, LLC (2015) The PyMOL Molecular Graphics System, Version 1.8.

Shaya D, Findeisen F, Abderemane-Ali F, Arrigoni C, Wong S, Nurva SR, Loussouarn G & Minor DL (2014) Structure of a Prokaryotic Sodium Channel Pore Reveals Essential Gating Elements and an Outer Ion Binding Site Common to Eukaryotic Channels. *Journal of Molecular Biology* 426: 467–483

Shimomura T, Yonekawa Y, Nagura H, Tateyama M, Fujiyoshi Y & Irie K (2020) A native prokaryotic voltage-dependent calcium channel with a novel selectivity filter sequence. *eLife* 9: e52828

Shorter E (2009) The history of lithium therapy. *Bipolar Disorders* 11: 4–9

Tang L, Gamal El-Din TM, Payandeh J, Martinez GQ, Heard TM, Scheuer T, Zheng N & Catterall WA (2014) Structural basis for Ca2+ selectivity of a voltage-gated calcium channel. *Nature* 505: 56–61

Tsai C-J, Tani K, Irie K, Hiroaki Y, Shimomura T, McMillan DG, Cook GM, Schertler GFX, Fujiyoshi Y & Li X-D (2013) Two Alternative Conformations of a Voltage-Gated Sodium Channel. *Journal of Molecular Biology* 425: 4074–4088

Ulmschneider MB, Bagnéris C, McCusker EC, DeCaen PG, Delling M, Clapham DE, Ulmschneider JP & Wallace BA (2013) Molecular dynamics of ion transport through the open conformation of a bacterial voltage-gated sodium channel. *Proc Natl Acad Sci USA* 110: 6364–6369

Verdolini N, Hidalgo-Mazzei D, Del Matto L, Muscas M, Pacchiarotti I, Murru A, Samalin L, Aedo A, Tohen M, Grunze H, *et al* (2021) Long-term treatment of bipolar disorder type I: A systematic and critical review of clinical guidelines with derived practice algorithms. *Bipolar Disorders* 23: 324–340

Winn MD, Ballard CC, Cowtan KD, Dodson EJ, Emsley P, Evans PR, Keegan RM, Krissinel EB, Leslie AGW, McCoy A, *et al* (2011) Overview of the *CCP* 4 suite and current developments. *Acta Crystallogr D Biol Crystallogr* 67: 235–242

Xia M, Liu H, Li Y, Yan N & Gong H (2013) The Mechanism of Na+/K+ Selectivity in Mammalian Voltage-Gated Sodium Channels Based on Molecular Dynamics Simulation.

Biophysical Journal 104: 2401–2409
Yamashita K, Hirata K & Yamamoto M (2018) *KAMO*: towards automated data processing for microcrystals. *Acta Crystallogr D Struct Biol* 74: 441–449
Yue L, Navarro B, Ren D, Ramos A & Clapham DE (2002) The Cation Selectivity Filter of the Bacterial Sodium Channel, NaChBac. *The Journal of General Physiology* 120: 845–853
Zakon HH (2012) Adaptive evolution of voltage-gated sodium channels: The first 800 million years. *Proc Natl Acad Sci USA* 109: 10619–10625